




A tuneable telecom wavelength entangled light emitting diode deployed in an installed fibre network

Zi-Heng Xiang^{1,2}, Jan Huwer ¹✉, Joanna Skiba-Szymanska¹, R. Mark Stevenson¹, David J. P. Ellis¹, Ian Farrer ^{2,3}, Martin B. Ward¹, David A. Ritchie ² & Andrew J. Shields¹

Entangled light emitting diodes based on semiconductor quantum dots are promising devices for security sensitive quantum network applications, thanks to their natural lack of multi-photon-pair generation. Apart from telecom wavelength emission, network integrability of these sources ideally requires electrical operation for deployment in compact systems in the field. For multiplexing of entangled photons with classical data traffic, emission in the telecom O-band and tuneability to the nearest wavelength channel in compliance with coarse wavelength division multiplexing standards (20 nm channel spacing) is highly desirable. Here we show a fully electrically operated telecom entangled light emitting diode with wavelength tuneability of more than 25 nm, deployed in an installed fibre network. With the source tuned to 1310.00 nm, we demonstrate multiplexing of true single entangled photons with classical data traffic and achieve entanglement fidelities above 94% on an installed fibre in a city.

¹Toshiba Europe Limited, Cambridge Research Laboratory, 208 Science Park, Milton Road, Cambridge CB4 0GZ, UK. ²University of Cambridge, Cavendish Laboratory, J.J. Thompson Avenue, Cambridge CB3 0HD, UK. ³Present address: Department of Electronic & Electrical Engineering, University of Sheffield, Sheffield S1 3JD, UK. ✉email: jan.huwer@crl.toshiba.co.uk

The success or failure of quantum light sources in advanced commercial photonic quantum-network applications is strongly dependent on integrability of these sources with current infrastructure and technology. Regarding networks, operation at telecom wavelength is as essential as wavelength tuneability, required for interfacing and multiplexing with other sources of classical or quantum light over the same optical fibre. In terms of quantum light emitters, scalable manufacturing techniques for their production as well as compliance with low voltage driving electronics for safe and long-term reliable operation in remote non-laboratory environments are most desirable.

Shared entanglement between distant network users is an important resource for quantum-network applications going beyond conventional quantum key distribution (QKD)¹ that makes use of weak coherent laser pulses^{2–4}. Greater robustness to photon number splitting attacks^{5,6}, an increase of communication distances⁷ and the prospect to link remote quantum processors⁸ are some of the immediate benefits. As currently employed sources are mostly based on spontaneous processes, intrinsically limiting efficiencies, further improvement is expected from sub-Poissonian photon-pair sources such as semiconductor quantum dots (QD), with the prospect for deterministic operation⁹. Such sources can also benefit highest level applications for scalable network architectures such as quantum relays¹⁰ and repeaters¹¹ based on teleportation and entanglement swapping protocols, posing further constraints on photon indistinguishability.

Quantum light sources based on III–V compound semiconductor QDs embedded in a positive-intrinsic-negative (p-i-n) diode⁹ are considered a promising approach in terms of scalable manufacturability as they are sharing the same material platform as standard laser diodes. These devices generate single entangled pairs of photons on the so-called biexciton cascade after electrical injection of carriers, which is why they are also referred to as entangled light emitting diodes (ELED)¹². Another approach for carrier injection is via optical excitation where one mainly distinguishes between non-resonant excitation above the bandgap of the surrounding semiconductor matrix and resonant excitation of the biexciton state¹³. The latter has recently become very popular, achieving good photon indistinguishabilities with high purity and most importantly, the potential for fully deterministic operation¹⁴. Recent progress in the field culminated in first demonstrations of entanglement swapping^{15,16} from this kind of source, an important step towards scalable quantum networks. However, these experiments require a sophisticated pulsed laser system combined with careful suppression of exciting laser light, making them at the moment not the first choice when it comes to field deployment of QD photon-pair sources in non-laboratory environments. In contrast, non-resonant excitation schemes are much simpler to implement and integrate, making them a welcome testbed for first steps into network integration of quantum light emitters. Of course, this comes at the expense of lower efficiency¹⁷ and photon purities, but with performances still good enough for experiments such as quantum teleportation with electrically¹⁸ and optically¹⁹ injected sources. For quantum communication applications, careful engineering of material compositions and wafer growth conditions have enabled fabrication of QDs emitting in the standard telecom wavelength bands^{20–23}, recently enabling for the first time the transmission of photons from a single quantum emitter over a deployed standard network fibre²⁴.

True network integration of quantum light sources requires co-existence with classical data traffic mostly in the telecom C-band over the same optical fibre. This favours operation of ELEDs in the telecom O-band as the large spectral separation combined with the generally reduced Raman scattering from the lower

energy C-band to the higher energy O-band makes wavelength division multiplexing of quantum light at the single-photon level with classical communication signals feasible^{25–27}. More sophisticated network architectures requiring higher bandwidth make use of the so-called coarse wavelength division multiplexing (CWDM) grid (ITU G.694.2), comprising a total of 18 channels from 1271 to 1611 nm with 20 nm spacing. For compatibility of ELEDs with this standard, spectral tuning ranges of 20 nm are desirable such that any emitter can be tuned to the closest CWDM channel or even changed to a different channel. Despite there has been good progress in the deterministic growth of QDs emitting at specific non-telecom wavelengths^{28,29}, post-growth tuning mechanisms remain most important for enhancing the yield in manufacturability of devices.

The application of magnetic fields³⁰ or strain^{31–35} has been demonstrated for tuning QD emission. While achieving only a few nanometres of tuneability, these approaches require large magnetic fields or very high voltages which is not practical for network deployment. In contrast, wavelength tuning via static electric fields^{36–38} is suitable for long-term safe operation, achieving good tuning ranges with only low applied voltages. In this work, we demonstrate a tuneable telecom ELED with low-voltage operation, large tuning range and strong single-photon character, which is compatible with networks containing classical communication traffic. This enables us to operate an ELED outside of a research laboratory and show sub-Poissonian entangled photon transmission with high fidelity multiplexed with classical data signals over the metropolitan fibre network in Cambridge.

Results

Tuneable ELED. A schematic of the tuneable device design is shown in Fig. 1a. Entangled photon pairs are emitted from the QDs located at the central circular region. These are optically excited by light emitted from the so-called ‘pumping diode’ surrounding it, when applying a forward bias to the top contact on the left. A reverse bias applied to the top contact from the inner diode is used to apply static fields for tuning the QD emission, making this the so-called ‘tuning diode’. The ring-circle structure enables homogeneous illumination of the tuning diode with pumping light from all sides. An optical microscope image of fabricated devices is shown in Fig. 1b. The central mesa for the design used in this work has a radius of 35 μm , typically containing around 120 QDs as can be seen in the camera image in Fig. 1c, showing luminescence of the QDs during operation of the device. Owing to the random nature of the type of self-assembled QDs used here, photons emitted at telecom wavelength generally exhibit a broad variation of parameters, requiring the selection of an emitter with suitable properties. For the device displayed, there is one QD meeting the requirements for brightness and entanglement fidelity. This is consistent with a typical yield of around 0.9% based on the examination of around 350 QDs.

The key features of the wafer structure are illustrated in Fig. 1d. The InAs/GaAs quantum dots used in this work were grown using the Stranski–Krastanov (S–K) growth mode in molecular beam epitaxy. Use of the so-called bi-modal growth mode²¹ results in QD emission in the telecom O-band. The QD layer is deposited on GaAs and capped with a thick layer of InGaAs (5 nm) which serves as optical pump and absorption layer, in contrast to structures operating at non-telecom wavelengths^{39,40}. The optically active part of the wafer is finished with another layer of GaAs, forming a quantum well (QW). Additional barriers made from AlGaAs grown below and above these central layers inhibit escape of charge carriers when applying electric fields along the vertical direction. The structure further contains

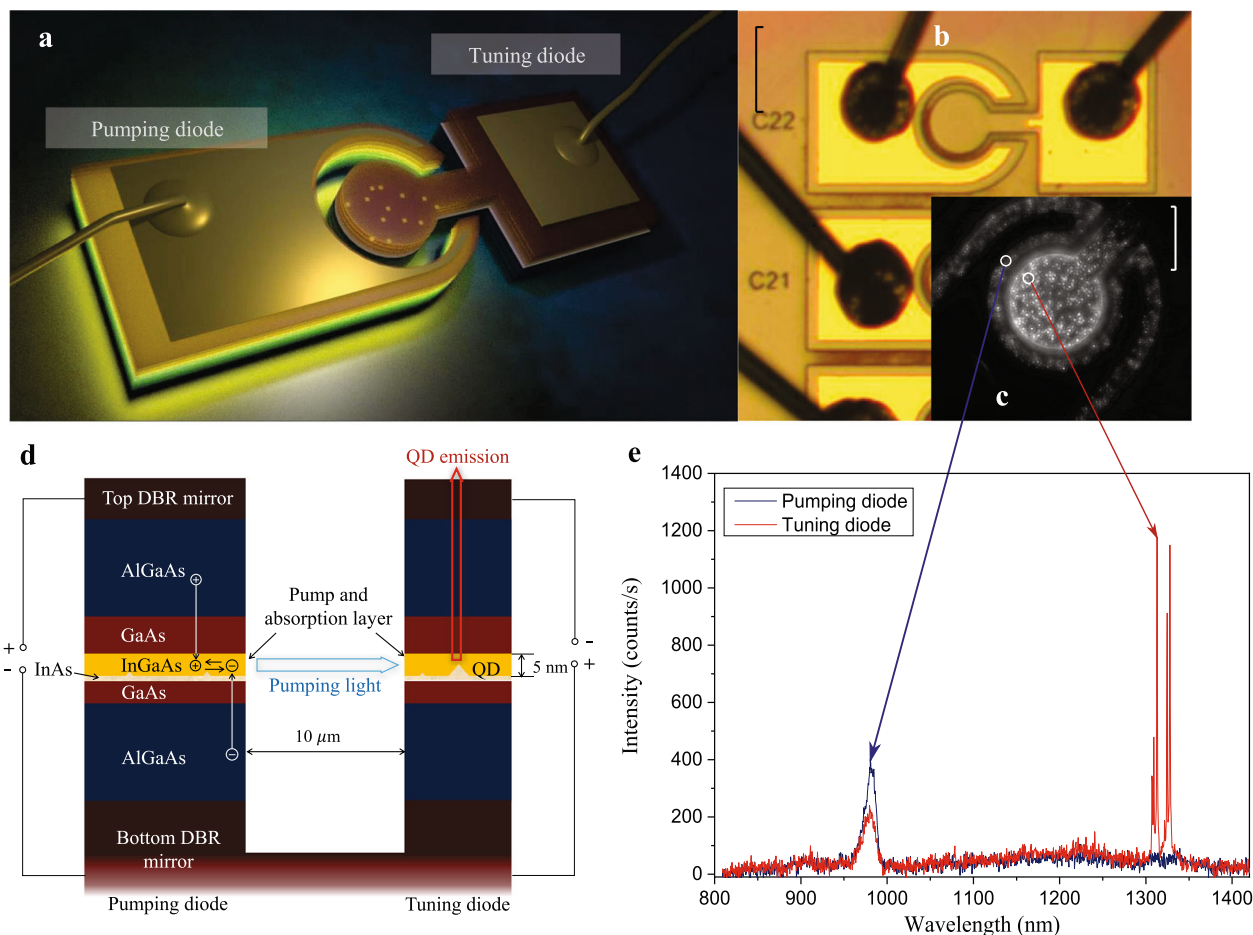


Fig. 1 Tuneable entangled light emitting diode. **a** Concept of device. A current is injected via the top contact on the pumping diode for optical excitation of single quantum dots in the embraced circular tuning diode. Both diodes share the same bottom contact not shown in the figure. **b** Microscope image of fabricated devices with attached bond wires. The displayed scale bar corresponds to 100 μm . **c** Microscope image of quantum dots (QD) in the structure emitting at telecom wavelength when applying a forward bias to the pumping diode. A long-pass filter at 1100 nm is placed before the camera to suppress short-wavelength pumping light for better visibility of QD emission. The displayed scale bar corresponds to 50 μm . **d** Layer structure of wafer. The central 5 nm InGaAs layer serves as pump and absorption layer for the on-chip optically excited device. It generates light at 950–1000 nm in the pumping diode (left) which is absorbed in the tuning diode (right), exciting QDs. The shown layer thicknesses are not to scale. DBR represents the distributed Bragg reflector. **e** Comparison of the spectrum of micro electro luminescence on the pumping diode (blue) and resulting micro photo luminescence from the tuning diode (red). The measurements were taken in a confocal microscope setup with collection from the top and a spot diameter of 2 μm .

stacked distributed Bragg reflector (DBR) mirrors made from GaAs/AlGaAs at the bottom and top, for enhancing the emission in the telecom O-band with a weak vertical half-wavelength ($\lambda/2$) cavity. The top three repeats of the bottom DBR are n-doped and the whole of the top DBR is p-doped (both with $2 \times 10^{18} \text{ cm}^{-3}$), with doping extending a few nanometres into the cavity layer from both sides, forming a p-i-n diode.

The combined optical pump and absorption layer is used for increasing the on-chip optical excitation efficiency. In the pumping diode, charge carriers are injected into the InGaAs QW when applying a forward bias across the p-i-n junction. Carrier recombination in this 2D layer gives rise to broadband optical emission around 980 nm as can be seen in the blue spectral curve displayed in Fig. 1e, measured in a confocal microscope setup from the top, on a position with no QD on the pumping diode. The spectral signal looks rather weak as this light is non-resonant with the embedded vertical cavity which favours in-plane rather than out-of-plane emission. Pumping light is absorbed by resonant optical excitation of confined states in the QW of the tuning diode. Here, carriers can recombine in QDs resulting in emission of single or entangled photons in the telecom O-band around 1310 nm along the vertical direction as

these are resonant with the embedded cavity. A corresponding spectrum is displayed as red curve in Fig. 1e. The geometric and extreme spectral separation of pumping light and QD emission of more than 300 nm enables an excellent suppression of background using standard optical filtering methods. This results in high-purity single-photon emission with values for zero time delay of the second-order correlation function ($g^{(2)}(0)$) well below 10%, which is comparable with other QD photon sources which are non-resonantly optically excited with an external laser^{22,35,36} (a measurement of second-order autocorrelation functions is shown in the Supplementary Fig. 1). In comparison with devices where the on-chip optical excitation is only based on conventional wetting layer emission and absorption (thickness < 1 nm), we observe a significantly enhanced efficiency of the optical pumping process (see Supplementary Note 1). This is most likely caused by increased absorption efficiency of pumping light due to the much higher thickness (5 nm) of the pump and absorption layer.

The AlGaAs barriers surrounding the QD layer as shown in Fig. 1d inhibit escape of charge carriers, enabling the application of large electrical fields across the p-i-n junction. Growth of the QDs in the InGaAs QW further loosens the confinement of

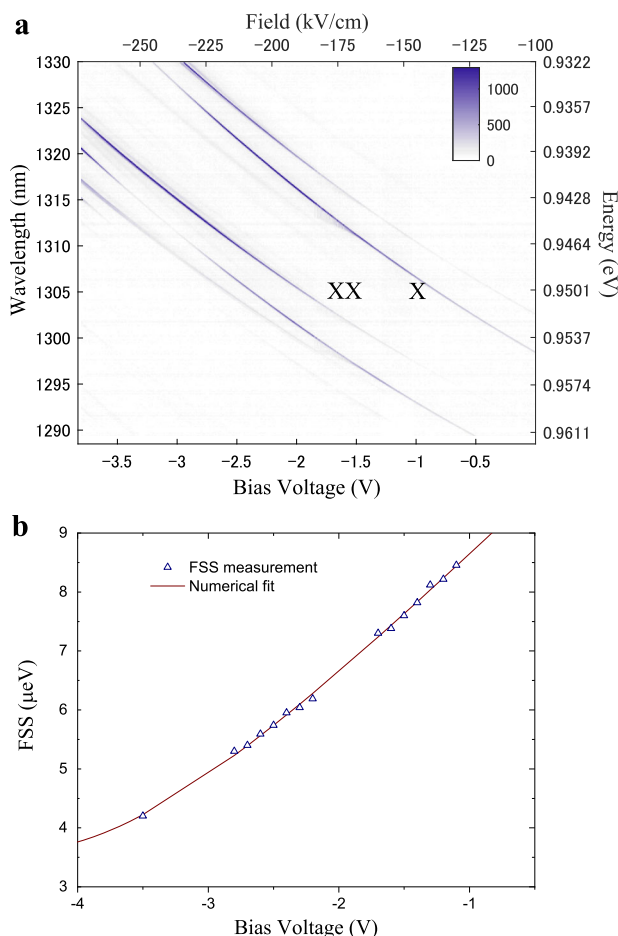


Fig. 2 Tuneability of photon emission. **a** Emission spectrum of on-chip optically excited single quantum dot (QD) as a function of applied bias voltage to the tuning diode. A wavelength shift of around 30 nm is observed for XX and X emission. **b** Corresponding change of the fine structure splitting (FSS) of the QD as a function of the applied bias. The values were extracted via a numerical fit to measured polarisation-filtered time-resolved photon-pair correlations. Error bars determined by the standard error from the numerical fit are negligible. The red curve is a numerical fit based on the theoretical model for dependence of the splitting due to the quantum confined Stark effect.

electron-hole pairs, resulting in a higher permanent dipole moment and polarizability of excitons, enhancing the tuneability of QD emission via the quantum confined Stark effect^{36,41,42}. In the following, we selected a single QD with good entanglement fidelity and intensity of emitted biexciton (XX) and exciton (X) photons. While photon indistinguishability from telecom S-K QDs with densities as used here is not sufficient for scalable quantum communication schemes, with radiative lifetimes around 1 ns and coherence times around 50 ps, it is not relevant for the present study, focussing on field deployment of a sub-Poissonian photon-pair source and network distribution of entanglement. Figure 2a shows wavelength tuneability of the emission spectrum when driving the pumping diode with a forward bias and changing the reverse bias on the tuning diode from -3.8 to 0 V. The neutral X and XX states can both be shifted over the center of the telecom O-band (1310 nm) with a maximum range of more than 25 nm for the applied voltages. This significantly exceeds the tuneability performance of short-wavelength devices^{36,39} and meets the requirements for compatibility with the ITU CWDM grid. It has to be emphasised that the electrical driving conditions for excitation are comparable with

directly electrically injected ELEDs¹² indicating the optimised operation of the tuneable devices while measured photon intensities are comparable with what is typically achieved with non-resonant optical excitation by an external laser with this type of telecom QDs.

We also observe the characteristic tuning of the fine structure splitting (FSS) of neutral X and XX states as a function of bias voltage, as shown in Fig. 2b. The splitting parameter was extracted from measurements of the time-resolved quantum beat of X-XX correlations when filtering both photons with a linear polarizer (for details see Supplementary Methods and Supplementary Fig. 2). For entangled photon-pair emission it is important to achieve FSS values of $10 \mu\text{eV}$ or less such that indistinguishability of the resulting two spectral components of a photon is guaranteed with typical detection setups featuring 100 ps timing resolution or better (see “Methods” for details). The splitting of the selected QD stays significantly below that threshold over the entire tuning range, meaning that the device maintains the condition for entangled photon-pair emission. In the remainder of the paper, we operate the device with a voltage of -2.6 V applied to the tuning diode, setting the XX emission to 1310.00 nm (the exact center of the O-band) and X emission to 1321.45 nm and resulting in an FSS of $5.6 \mu\text{eV}$.

Field deployment. Simple electrical operation and compatibility with wavelength division multiplexing standards allow us for the first time to demonstrate the deployment and telecommunication network integration of the device. We operate a fully remotely controlled system that is installed in an office at a location in West Cambridge (CAM), which is connected via the Cambridge Network with two optical fibres of 15 km length each to the Toshiba Cambridge Research Laboratory (CRL) in the Science Park. Figure 3 shows the overall experimental setup and a map of Cambridge. The system consists of multiple sub-systems: an entangled photon transmission module containing the tuneable ELED, a spectral filter with polarisation reference for detector calibration, a polarisation stabilisation module and a quantum/classical data multiplexing module.

The ELED device is mounted in a closed-cycle cryostat, cooling it to 6 K. The emitted light from the quantum dot is coupled into single mode optical fibre and sent to a spectral filter module mounted in an instrument rack. Here, a diffraction grating is used to separate the entangled X and XX photons into two different output modes. Right after the spectral filter, the X photons pass through a polarisation discrimination setup that consists of a half waveplate (HWP), a quarter waveplate (QWP) and a linear polariser (LP), projecting their quantum state into different polarisation bases at the remote location before transmission to CRL for detection. The entangled XX partner photons are sent to CRL over a separate network fibre which is stabilized for changes of birefringence (see “Methods”) and additionally hosts a classical data connection for remote control of the deployed system. At CRL, their polarisation state is projected using an electronic polarisation controller (EPC) and a fibre polarizing beam splitter (PBS). Single-photon arrival times for X and XX photons are recorded using superconducting nanowire single-photon detectors (Single Quantum) and photon-pair correlations in different detection bases are measured for evaluation of the entanglement fidelity across the 15-km fibre link (see “Methods”).

A precise alignment of the detection basis to the eigenbasis of the QD emission is essential in these experiments. In this work, we make use of an innovative method for the precise measurement of said eigenbasis, that is based on analysing time-resolved photon-pair correlations in a set of randomly oriented detection bases (see “Methods”). For detector calibration, polarisation reference light is

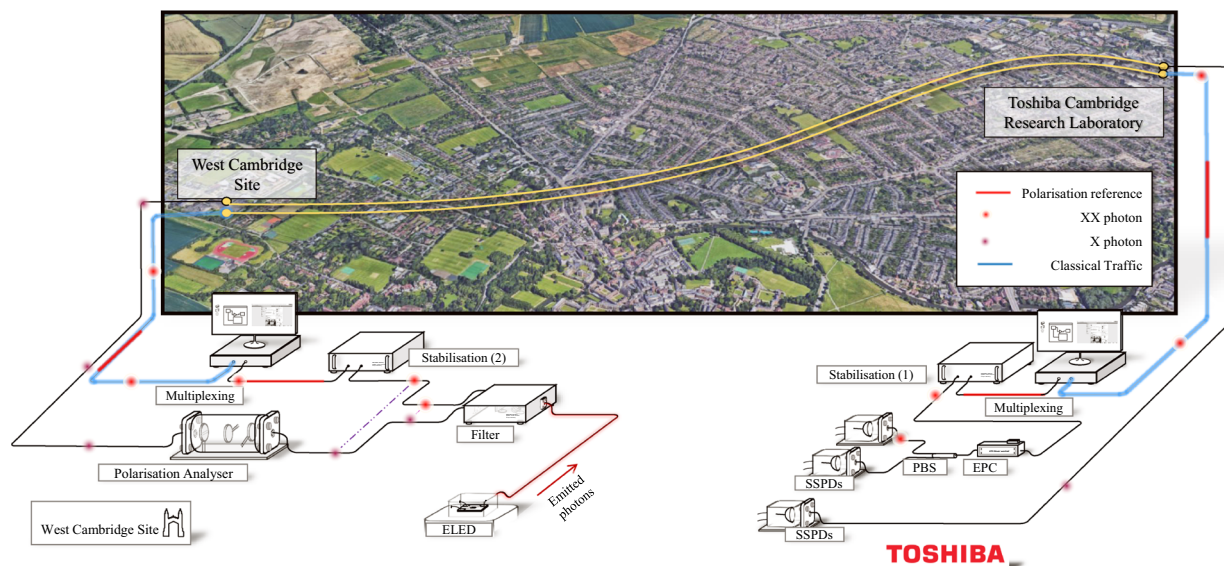


Fig. 3 Schematic of overall experimental setup for entangled photon transmission from network deployed entangled light emitting diode. Optical signals from three sub-systems are sent over the network. Single photons are shown as ‘red’ (XX) and ‘violet’ (X) dots, laser pulses for polarisation stabilisation are shown as short ‘red’ lines and classical data traffic is shown as continuous ‘blue’ line. Entangled photon pairs are generated from the tuneable entangled light emitting diode at West Cambridge. X and XX photons are spatially separated with a spectral filter module. X photons pass through a polarisation analyser consisting of a half waveplate (HWP), a quarter waveplate (QWP) and a linear polariser (LP) before being sent over one of the two installed fibres. Entangled XX photons are sent over the other field fibre which is stabilised for polarisation drifts using a polarisation stabilisation sub-system (Stabilisation 1 and 2). At the Cambridge Research Laboratory (CRL), their quantum state is measured using an electronic polarisation controller (EPC), a polarising beam splitter (PBS) and two superconducting single-photon detectors (SSPDs). For remote control of the deployed source and system components, a classical data connection in the telecom C-band is established over the same fibre using a classical-quantum multiplexing system (labelled as Multiplexing). Arrival time of the X photons in the first fibre is measured with a third SSPD at CRL. Map: Imagery ©2019 Google, Getmapping plc, Infoterra Ltd and Bluesky, The GeoInformation Group, Maxar Technologies, Data SIO, NOAA, U.S. Navy, NGA, GEBCO, Maxar Technologies, Landsat/Copernicus, Map data ©2019.

injected into X and XX output modes from the spectral filter module, more details are provided in the Supplementary Methods and Supplementary Figs. 2 and 3.

For demonstrating true network integration, the entangled quantum bits are multiplexed with classical communication traffic over the same optical fibre using CWDM with quantum light at 1310 nm and a bidirectional 1Gbit data connection at 1550 nm (see “Methods”). Previous field trials have illustrated the feasibility of multiplexing QKD qubits based on attenuated laser pulses with classical data traffic over installed network links^{43–45}. However, the co-existence of entangled qubits from a sub-Poissonian photon source and classical data traffic over a real-world network has not been demonstrated yet. The classical communication channel is used to remotely control the ELED system, the polarisation stabilisation system and data acquisition during the experiments. Figure 4 shows a comparison of the single-photon purity of quantum light from the ELED before and after transmission over the lit field fibre, by measuring the second-order autocorrelation function. After transmission, the light is still strongly anti-bunched with a $g^{(2)}(0)$ value of 0.26 being significantly below the classical limit of 0.50. A more detailed analysis reveals that the increase from the laboratory-measured value of 0.08 is primarily caused by a reduction of the signal-to-background ratio due to photon loss in the network fibre and all system components, and not the presence of the classical data link (see Supplementary Note 2).

Discussion

Figure 5a–c shows the results for co- and cross-polarised coincidences in the horizontal/vertical (HV), diagonal/anti-diagonal (DA) and right-/left-circular (RL) basis when projecting the

quantum states of X photons at CAM and XX photons at CRL. The detection basis was changed every 10 min. In the HV basis, we observe a strong correlation of photon polarisations with a maximum contrast of 94.5%. The superposition bases DA and RL show high contrast quantum correlations as well, with the characteristic beat owing to the FSS of the QD as reported multiple times before^{21,46,47}. The fidelity to the maximally entangled Bell ϕ^+ state peaks at $94.4 \pm 0.3\%$ (see Fig. 5d) for a post-selection window size of 48 ps. This compares well with a maximum fidelity of 97.3% measured in a laboratory environment before deployment. The small drop in fidelity is mainly due to a decrease in signal-to-background when sending the photons over installed fibre. To demonstrate the good stability of the deployed ELED device, the experiment was continuously running over a period of 40 h. Figure 5e shows the evolution of the entanglement fidelity based on 120 min of data per displayed point. The bottom of the graph shows the corresponding quantum-bit error rate which is stable around 3.8%. These results are directly obtained from raw data and no background subtraction of any kind has been done during processing. The classical communication link was running at all times. For a post-selection window of 200 ps, which is well above gate widths of commonly used communication-grade detector systems⁴⁸, the maximum fidelity after transmission over the network fibre is $91.9 \pm 0.2\%$, still more than 190 standard deviations above the classical limit.

To conclude, we have developed the first electrically operated tuneable ELED emitting in the main telecommunication wavelength band suitable for multiplexing with classical communication signals. Combination of on-chip optical excitation with dedicated layer structure and device design enable low-voltage operation (<5 V) and large wavelength tuneability (>25 nm). A high single-photon purity compatible with typical non-resonantly

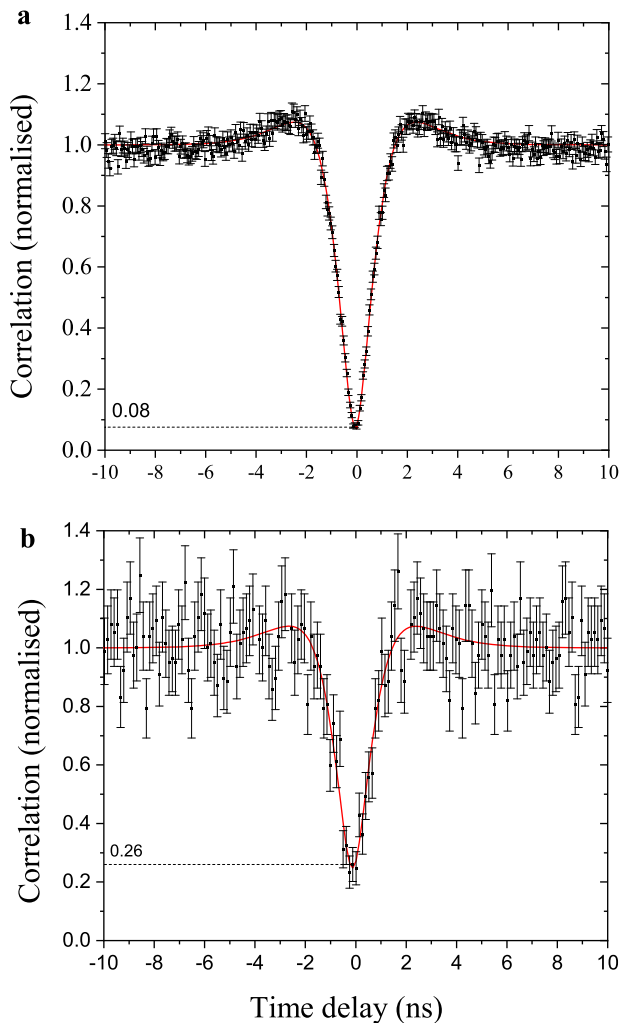


Fig. 4 Single-photon transmission. Second-order autocorrelation measurement result for XX photons **a** in the laboratory and **b** after transmission over 15 km of installed fibre, multiplexed with classical data traffic. Data acquisition times were 5 min and 30 min, respectively. The red curves show a theoretical fitting function which is used to extract the displayed $g^{(2)}(0)$ values and corresponding background contribution. Displayed error bars are propagated from Poissonian counting statistics.

excited QD light sources was observed and entanglement with a fidelity of more than 94% was achieved after integration and deployment in a real-world fibre network. Continuous operation of the source showed stable entanglement over 15 km of installed fibre shared with classical data traffic used for remote control of all system components.

Compatibility of the device with standard low-voltage power supplies and compliance with laser-safety standards due to exclusively electrical operation pave the way for future integration of devices based on this approach in various end user applications. The large wavelength tuneability furthermore opens up the route for flexible wavelength division multiplexing of multiple tuneable ELED sources over the same optical network links and most importantly, multiplexing with classical data channels. This is of fundamental importance for the low-cost integration of quantum networks in classical network infrastructures.

While the reported results provide a proof-of-principle demonstration of practicality of the technology for network deployment, further work is required to make devices based on on-chip optical excitation that are suitable for high-level quantum-network applications. These are expected to require pulsed

operation at GHz clock rates, high source efficiencies and good photon indistinguishability. Pulsed high-frequency operation is achievable via a reduction of the device capacitance by simply shrinking the dimensions of the pumping diode. Higher photon collection efficiencies could be achieved by implementing nano-photonic structures such as in-plane circular Bragg reflectors^{49–51}, broadband optical antennas⁵² or microlenses⁵³ while charge control of QDs⁵⁴ via optimisation of the tuning diode might open up the route for higher photon generation efficiencies as required for deterministic operation. Furthermore, QDs grown by so-called droplet epitaxy are a highly promising alternative to S–K grown QDs as they show extremely good coherence properties even for non-resonant optical excitation¹⁹.

Methods

Calibration of detector polarisation basis. The measurement of the orientation of the linear QD eigenbasis is usually done by maximising the spectral shift of entangled photons when detecting after a rotatable LP. This generally requires placement of the polariser before light is coupled from the QD emitter into the first single-mode fibre⁵⁵ which is not practical in compact setups. The following method that we employed is compatible with devices where free-space access to emitted photons on top of the emitter chip is not possible. We take X–XX correlation measurements (co- and cross-polarised) in three arbitrary but linearly independent detection bases. As explained in more detail in the Supplementary Methods, the time-dependent evolution of the correlation signal is then used to extract the exact orientation of the eigenbasis of QD emission in the chosen detector basis orientation. Using the standard procedure for Müller matrix evaluation⁵⁶, this allows us to calculate the transformation between the two reference frames. In a second step, this information is used for calibrating the detection basis by injection of properly oriented polarisation reference states for a perfect match with the eigenbasis of QD emission.

Measurement of entanglement. Two-photon correlations between X and XX photons are measured with a single correlator at CRL, providing intrinsic synchronisation. Entanglement measurements are carried out by recording photon-pair correlations c_{PQ} for co- and cross-polarized case in the three principal detection bases HV, DA and RL. The fidelity to the maximally entangled Bell ϕ^+ state is then calculated as $\mathcal{F} = (1 + C_{HV} + C_{DA} - C_{RL})/4$, where C_{PQ} are the so-called correlation coefficients with $C_{PQ} = (c_{PP} - c_{PQ})/(c_{PP} + c_{PQ})$.

FSS threshold for observation of entanglement. The entanglement fidelity follows a sinusoidal oscillation with the period given by h/δ (see Supplementary Methods) with δ being the FSS of the exciton level. Assuming that other dephasing processes are negligible at short time scales, for an ideal emitter the oscillation will cause the fidelity to drop to 50% (the classical limit) after a quarter of the rotation period. Therefore, as a general rule of thumb, for observing entanglement, the detector timing resolution should be equal to or better than this limit. Assuming a typical timing resolution of 100 ps, this results in a maximum affordable splitting parameter of $\delta \approx 10 \mu\text{eV}$.

Polarisation stabilisation system. The use of polarisation qubits over long installed fibre requires the stabilisation of changes in birefringence that naturally occur due to changing environmental conditions. Similar to our previous work²⁴ we make use of a time-multiplexed polarisation stabilisation system operating at the XX photon wavelength of 1310 nm. Every 15 s, two polarisation references that are aligned along orthogonal axes on the Poincaré sphere are injected for 100 ms and measured over the field fibre. Feedback to a polarisation controller is then applied to compensate for detected polarisation rotations. In addition, the stabilisation is forced every 225 s and typically takes around 3 s to reach maximum alignment. The resulting overall duty-cycle for transmission of quantum bits is around 98%.

Classical-quantum multiplexing. A bidirectional 1 Gbit classical communication link is established with standard 1550 nm transceiver modules. Up- and down-stream traffic is isolated by directional filtering, using circulators. Multiple CWDM modules in the quantum and classical channels and a diffraction grating spectral filter with a full width at half maximum of less than 1 nm installed in the quantum channel at CRL, are used to suppress the background from the classical light to a very low level. More details about this part of the experimental setup can be found in the Supplementary Note 3 and Supplementary Fig. 4.

Loss information. The main optical path used for distributing the entangled photons goes through the polarisation stabilisation and classical communication multiplexing modules on both ends of the installed fibre. Including the additional filter at the receiver required to block residual light from the classical communication, and the EPC and PBS before the detectors, the total loss amounts to

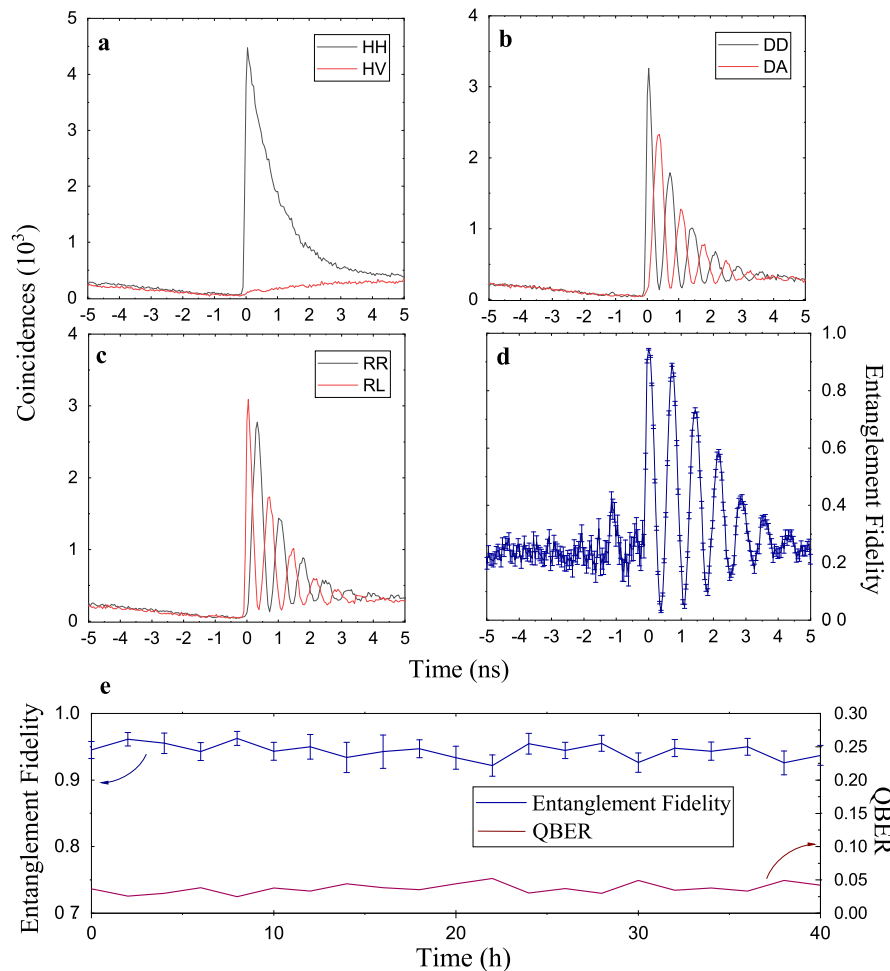


Fig. 5 Correlation measurements of entangled photons across installed network link. a Horizontal-horizontal (HH) and horizontal-vertical (HV) polarisation detection. **b** Diagonal-diagonal (DD) and diagonal-anti-diagonal (DA) polarisation detection. **c** Right-right- (RR) and right-left-hand circular (RL) polarisation detection. **d** Fidelity to Bell ϕ^+ state. Data is displayed on 48 ps resolution timing grid. **e** Evolution of maximum fidelity and corresponding quantum bit error rate (QBER) over 40 h of continuous operation. Each data point corresponds to 2 h of data. All displayed error bars indicate one standard deviation propagated from Poissonian counting statistics.

3.3 dB for the transmission at 1310 nm. The fibre connection from the remote location at CAM to CRL has an overall length of 15 km and is partially privately owned and partially part of the University Network. The connection for transmitting entangled XX photons and establishing classical communication has a total loss of 8.5 dB at 1310 nm and the fibre used for sending the projected X photons has a loss of 12.5 dB. The latter is most likely caused by a sharp bent of the fibre cable in one of the multiple network nodes that the connection is routed through. In this fibre, we additionally experienced leakage of classical transceiver light at 1309 and 1313 nm probably from a neighbouring strand in the same optical cable. This required additional filtering of received X photons at 1321.45 nm at CRL using a tuneable narrowband filter, adding 2.5 dB to the overall loss budget.

Photon rates. Photon pairs emitted from the ELED are coupled into single-mode optical fibre using a confocal microscope setup with an estimated extraction efficiency into the fibre around 3%. The raw rate of detected XX photons and X photons before transmission over the network fibre are 500 and 400 kHz, respectively, when driving the tuneable ELED with a DC current. At the output of the field fibre and the multiple system modules, we detect XX photon rates of 33 kHz. The detected X photon rate is around 13 kHz after sending the projected qubits to CRL over the high-loss fibre.

Data availability

The datasets generated during and/or analysed during the current study are available from the corresponding author on reasonable request.

Received: 19 February 2020; Accepted: 8 June 2020;

Published online: 03 July 2020

References

- Shor, P. W. & Preskill, J. Simple proof of security of the BB84 quantum key distribution protocol. *Phys. Rev. Lett.* **85**, 441 (2000).
- Lo, H.-K., Ma, X. & Chen, K. Decoy state quantum key distribution. *Phys. Rev. Lett.* **94**, 230504 (2005).
- Lo, H.-K., Curty, M. & Qi, B. Measurement-device-independent quantum key distribution. *Phys. Rev. Lett.* **108**, 130503 (2012).
- Sasaki, M. et al. Field test of quantum key distribution in the Tokyo QKD Network. *Opt. Express* **19**, 10387–10409 (2011).
- Ekert Quantum cryptography based on Bell's theorem. *Phys. Rev. Lett.* **67**, 661–663, <https://doi.org/10.1103/PhysRevLett.67.661> (1991).
- Ursin, R. et al. Entanglement-based quantum communication over 144 km. *Nat. Phys.* **3**, 481 (2007).
- Yin, J. et al. Satellite-based entanglement distribution over 1200 kilometers. *Science* **356**, 1140–1144, <https://doi.org/10.1126/science.aan3211> (2017).
- Kimble, H. J. The quantum internet. *Nature* **453**, 1023 (2008).
- Benson, O., Santori, C., Pelton, M. & Yamamoto, Y. Regulated and entangled photons from a single quantum dot. *Phys. Rev. Lett.* **84**, 2513 (2000).
- Jacobs, B. C., Pittman, T. B. & Franson, J. D. Quantum relays and noise suppression using linear optics. *Phys. Rev. A* **66**, 46, <https://doi.org/10.1103/PhysRevA.66.052307> (2002).
- Briegleb, H.-J., Dür, W., Cirac, J. I. & Zoller, P. Quantum Repeaters: The Role of Imperfect Local Operations in Quantum Communication. *Phys. Rev. Lett.* **81**, 5932–5935, <https://doi.org/10.1103/PhysRevLett.81.5932> (1998).
- Salter, C. L. et al. An entangled-light-emitting diode. *Nature* **465**, 594 (2010).
- Müller, M., Bounouar, S., Jöns, K. D., Glässl, M. & Michler, P. On-demand generation of indistinguishable polarization-entangled photon pairs. *Nat. Photon* **8**, 224–228, <https://doi.org/10.1038/nphoton.2013.377> (2014).

14. Reindl, M. et al. All-photonic quantum teleportation using on-demand solid-state quantum emitters. *Sci. Adv.* **4**, eaau1255, <https://doi.org/10.1126/sciadv.aau1255> (2018).
15. Basso Basset, F. et al. Entanglement swapping with photons generated on demand by a quantum dot. *Phys. Rev. Lett.* **123**, 160501, <https://doi.org/10.1103/PhysRevLett.123.160501> (2019).
16. Zopf, M. et al. Entanglement swapping with semiconductor-generated photons violates bell's inequality. *Phys. Rev. Lett.* **123**, 160502, <https://doi.org/10.1103/PhysRevLett.123.160502> (2019).
17. Strauf, S. et al. High-frequency single-photon source with polarization control. *Nat. Photon* **1**, 704–708, <https://doi.org/10.1038/nphoton.2007.227> (2007).
18. Varnava, C. et al. An entangled-LED-driven quantum relay over 1 km. *npj Quantum Inf.* **2**, 145, <https://doi.org/10.1038/npjqi.2016.6> (2016).
19. Anderson, M. et al. Quantum teleportation using highly coherent emission from telecom C-band quantum dots. *npj Quantum Inf.* **6**, 1023, <https://doi.org/10.1038/s41534-020-0249-5> (2020).
20. Zinoni, C. et al. Time-resolved and antibunching experiments on single quantum dots at 1300 nm. *Appl. Phys. Lett.* **88**, 131102 (2006).
21. Ward, M. B. et al. Coherent dynamics of a telecom-wavelength entangled photon source. *Nat. Commun.* **5**, 3316 (2014).
22. Müller, T. et al. A quantum light-emitting diode for the standard telecom window around 1550 nm. *Nat. Commun.* **9**, 862 (2018).
23. Kors, A., Reithmaier, J. P. & Benyoucef, M. Telecom wavelength single quantum dots with very small excitonic fine-structure splitting. *Appl. Phys. Lett.* **112**, 172102, <https://doi.org/10.1063/1.5023184> (2018).
24. Xiang, Z.-H. et al. Long-term transmission of entangled photons from a single quantum dot over deployed fiber. *Sci. Rep.* **9**, 4111 (2019).
25. Chapuran, T. E. et al. Optical networking for quantum key distribution and quantum communications. *N. J. Phys.* **11**, 105001 (2009).
26. Choi, I., Young, R. J. & Townsend, P. D. Quantum information to the home. *N. J. Phys.* **13**, 63039 (2011).
27. Ciurana, A. et al. Quantum metropolitan optical network based on wavelength division multiplexing. *Opt. Express* **22**, 1576–1593 (2014).
28. Jahn, J.-P. et al. An artificial Rb atom in a semiconductor with lifetime-limited linewidth. *Phys. Rev. B* **92**, 245439 (2015).
29. Keil, R. et al. Solid-state ensemble of highly entangled photon sources at rubidium atomic transitions. *Nat. Commun.* **8**, 15501 (2017).
30. Schulhauser, C. et al. Magneto-optical properties of charged excitons in quantum dots. *Phys. Rev. B* **66**, 193303 (2002).
31. Zhang, J. et al. High yield and ultrafast sources of electrically triggered entangled-photon pairs based on strain-tunable quantum dots. *Nat. Commun.* **6**, 10067 (2015).
32. Bonato, C. et al. Strain tuning of quantum dot optical transitions via laser-induced surface defects. *Phys. Rev. B* **84**, 75306 (2011).
33. Chen, Y. et al. Wavelength-tunable entangled photons from silicon-integrated III-V quantum dots. *Nat. Commun.* **7**, 10387 (2016).
34. Jöns, K. D. et al. Dependence of the redshifted and blueshifted photoluminescence spectra of single In x Ga 1-x As/GaAs quantum dots on the applied uniaxial stress. *Phys. Rev. Lett.* **107**, 217402 (2011).
35. Zeuner, K. D. et al. A stable wavelength-tunable triggered source of single photons and cascaded photon pairs at the telecom C-band. *Appl. Phys. Lett.* **112**, 173102 (2018).
36. Patel, R. B. et al. Two-photon interference of the emission from electrically tunable remote quantum dots. *Nat. Photonics* **4**, 632 (2010).
37. Oulton, R. et al. Manipulation of the homogeneous linewidth of an individual In (Ga) As quantum dot. *Phys. Rev. B* **66**, 45313 (2002).
38. Findeis, F., Baier, M., Beham, E., Zrenner, A. & Abstreiter, G. Photocurrent and photoluminescence of a single self-assembled quantum dot in electric fields. *Appl. Phys. Lett.* **78**, 2958–2960 (2001).
39. Lee, J. P. et al. Electrically driven and electrically tunable quantum light sources. *Appl. Phys. Lett.* **110**, 71102 (2017).
40. Munnely, P. et al. Electrically tunable single-photon source triggered by a monolithically integrated quantum dot microlaser. *ACS Photonics* **4**, 790–794 (2017).
41. Miller, D. A. B. et al. Band-edge electroabsorption in quantum well structures: the quantum-confined Stark effect. *Phys. Rev. Lett.* **53**, 2173 (1984).
42. Laucht, A. et al. Electrical control of spontaneous emission and strong coupling for a single quantum dot. *N. J. Phys.* **11**, 23034 (2009).
43. Townsend, P. D. Simultaneous quantum cryptographic key distribution and conventional data transmission over installed fibre using wavelength-division multiplexing. *Electron. Lett.* **33**, 188–190 (1997).
44. Mao, Y. et al. Integrating quantum key distribution with classical communications in backbone fiber network. *Opt. express* **26**, 6010–6020 (2018).
45. Choi, I. et al. Field trial of a quantum secured 10 Gb/s DWDM transmission system over a single installed fiber. *Opt. express* **22**, 23121–23128 (2014).
46. Stevenson, R. M. et al. Evolution of entanglement between distinguishable light states. *Phys. Rev. Lett.* **101**, 170501 (2008).
47. Akopian, N. et al. Entangled photon pairs from semiconductor quantum dots. *Phys. Rev. Lett.* **96**, 130501 (2006).
48. Yuan, Z. L., Kardynal, B. E., Sharpe, A. W. & Shields, A. J. High speed single photon detection in the near infrared. *Appl. Phys. Lett.* **91**, 41114, <https://doi.org/10.1063/1.2760135> (2007).
49. Liu, J. et al. A solid-state source of strongly entangled photon pairs with high brightness and indistinguishability. *Nature Nanotechnology*; <https://doi.org/10.1038/s41565-019-0435-9> (2019).
50. Rickert, L., Kupko, T., Rodt, S., Reitzenstein, S. & Heindel, T. Optimized designs for telecom-wavelength quantum light sources based on hybrid circular Bragg gratings. *Opt. Express* **27**, 36824–36837, <https://doi.org/10.1364/OE.27.036824> (2019).
51. Wang, H. et al. On-demand semiconductor source of entangled photons which simultaneously has high fidelity, efficiency, and indistinguishability. *Phys. Rev. Lett.* **122**, 113602, <https://doi.org/10.1103/PhysRevLett.122.113602> (2019).
52. Chen, Y., Zopf, M., Keil, R., Ding, F. & Schmidt, O. G. Highly-efficient extraction of entangled photons from quantum dots using a broadband optical antenna. *Nat. Commun.* **9**, 2994, <https://doi.org/10.1038/s41467-018-05456-2> (2018).
53. Gschrey, M. et al. Highly indistinguishable photons from deterministic quantum-dot microlenses utilizing three-dimensional in situ electron-beam lithography. *Nat. Commun.* **6**, 7662, <https://doi.org/10.1038/ncomms8662> (2015).
54. Young, R. J. et al. Controlling the polarization correlation of photon pairs from a charge-tunable quantum dot. *Appl. Phys. Lett.* **91**, 11114, <https://doi.org/10.1063/1.2754641> (2007).
55. Young, R. J. et al. Improved fidelity of triggered entangled photons from single quantum dots. *N. J. Phys.* **8**, 29 (2006).
56. Layden, D., Wood, M. F. G. & Vitkin, I. A. Optimum selection of input polarization states in determining the sample Mueller matrix: a dual photoelastic polarimeter approach. *Opt. Express* **20**, 20466–20481 (2012).

Acknowledgements

The authors would like to thank A. J. Bennett and J. Dynes for technical discussions and A. Wonfor for arranging access to the fibre network. The authors acknowledge partial financial support from the Engineering and Physical Sciences Research Council, and the EPSRC Quantum Technology Hubs in Quantum Communications. Z.-H.X. would like to show his gratitude to the Cambridge Trust, China Scholarship Council and Toshiba Europe Limited for the financial support of his Ph.D. programme.

Author contributions

Devices were developed by Z.-H.X., J.S.-S., D.J.P.E. and J.H. and processed by Z.-H.X. and J.S.-S. on a wafer developed and grown by M.B.W., I.F. and D.A.R.; Z.-H.X. and J.H. designed and built the experiment and acquired the data; Z.-H.X. and J.H. analysed the data with contribution from R.M.S.; R.M.S. and A.J.S. guided the work. All authors discussed the experiments, results and their interpretation. J.H. and Z.-H.X. wrote the paper with input from all co-authors.

Competing interests

The authors declare no competing interests.

Additional information

Supplementary information is available for this paper at <https://doi.org/10.1038/s42005-020-0390-7>.

Correspondence and requests for materials should be addressed to J.H.

Reprints and permission information is available at <http://www.nature.com/reprints>

Publisher's note Springer Nature remains neutral with regard to jurisdictional claims in published maps and institutional affiliations.



Open Access This article is licensed under a Creative Commons Attribution 4.0 International License, which permits use, sharing, adaptation, distribution and reproduction in any medium or format, as long as you give appropriate credit to the original author(s) and the source, provide a link to the Creative Commons license, and indicate if changes were made. The images or other third party material in this article are included in the article's Creative Commons license, unless indicated otherwise in a credit line to the material. If material is not included in the article's Creative Commons license and your intended use is not permitted by statutory regulation or exceeds the permitted use, you will need to obtain permission directly from the copyright holder. To view a copy of this license, visit <http://creativecommons.org/licenses/by/4.0/>.

© The Author(s) 2020